NASA/TP-2003-212140

InGaAsSb Detectors' Characterization for 2-μm CO_2 Lidar/DIAL Applications

Tamer F. Refaat
Science and Technology Corporation, Hampton, Virginia

M. Nurul Abedin, Grady J. Koch, and Upendra N. Singh
Langley Research Center, Hampton, Virginia

February 2003

The NASA STI Program Office . . . in Profile

Since its founding, NASA has been dedicated to the advancement of aeronautics and space science. The NASA Scientific and Technical Information (STI) Program Office plays a key part in helping NASA maintain this important role.

The NASA STI Program Office is operated by Langley Research Center, the lead center for NASA's scientific and technical information. The NASA STI Program Office provides access to the NASA STI Database, the largest collection of aeronautical and space science STI in the world. The Program Office is also NASA's institutional mechanism for disseminating the results of its research and development activities. These results are published by NASA in the NASA STI Report Series, which includes the following report types:

- TECHNICAL PUBLICATION. Reports of completed research or a major significant phase of research that present the results of NASA programs and include extensive data or theoretical analysis. Includes compilations of significant scientific and technical data and information deemed to be of continuing reference value. NASA counterpart of peer-reviewed formal professional papers, but having less stringent limitations on manuscript length and extent of graphic presentations.

- TECHNICAL MEMORANDUM. Scientific and technical findings that are preliminary or of specialized interest, e.g., quick release reports, working papers, and bibliographies that contain minimal annotation. Does not contain extensive analysis.

- CONTRACTOR REPORT. Scientific and technical findings by NASA-sponsored contractors and grantees.

- CONFERENCE PUBLICATION. Collected papers from scientific and technical conferences, symposia, seminars, or other meetings sponsored or co-sponsored by NASA.

- SPECIAL PUBLICATION. Scientific, technical, or historical information from NASA programs, projects, and missions, often concerned with subjects having substantial public interest.

TECHNICAL TRANSLATION. English-language translations of foreign scientific and technical material pertinent to NASA's mission.

Specialized services that complement the STI Program Office's diverse offerings include creating custom thesauri, building customized databases, organizing and publishing research results . . . even providing videos.

For more information about the NASA STI Program Office, see the following:

- Access the NASA STI Program Home Page at ***http://www.sti.nasa.gov***

- Email your question via the Internet to help@sti.nasa.gov

- Fax your question to the NASA STI Help Desk at (301) 621-0134

- Telephone the NASA STI Help Desk at (301) 621-0390

- Write to:
  NASA STI Help Desk
  NASA Center for AeroSpace Information
  7121 Standard Drive
  Hanover, MD 21076-1320

NASA/TP-2003-212140

InGaAsSb Detectors' Characterization for 2-μm CO_2 Lidar/DIAL Applications

Tamer F. Refaat
Science and Technology Corporation, Hampton, Virginia

M. Nurul Abedin, Grady J. Koch, and Upendra N. Singh
Langley Research Center, Hampton, Virginia

National Aeronautics and
Space Administration

Langley Research Center
Hampton, Virginia 23681-2199

February 2003

Acknowledgments

The authors would like to thank the Earth Sciences Technology Office (ESTO) at NASA Goddard Space Flight Center for financial support of 2-μm detector development at NASA Langley Research Center. The authors would like to extend their acknowledgments to Dr. Syed Ismail for his suggestions and discussions on the science of 2-μm Lidar/ DIAL remote sensing for monitoring the atmospheric constituents. Thanks also go to Oleg V. Sulima, Michael Mauk, and Louis DiNetta of AstroPower, Inc. Their help and discussion about InGaAsSb detectors are very much appreciated.

Available from:

NASA Center for AeroSpace Information (CASI)
7121 Standard Drive
Hanover, MD 21076-1320
(301) 621-0390

National Technical Information Service (NTIS)
5285 Port Royal Road
Springfield, VA 22161-2171
(703) 605-6000

Abstract

Recent interest in monitoring atmospheric carbon dioxide focuses attention on infrared remote sensing using the 2-μm lidar/differential absorption lidar (DIAL) technique. Quantum detectors are critical components in this technique, and many research efforts concentrate on developing such devices for the 2-μm wavelength. In this report, the characterization results of InGaAsSb quantum detectors for the 2-μm wavelength range are presented, including the experimental setup and procedure. The detectors are prototype devices manufactured by using separate absorption and multiplication (SAM) structures. The characterization experiments include voltage-current (V-I) measurements, spectral response and its variation with bias voltage and temperature, noise measurements, noise-equivalent-power (NEP) and detectivity calculations, and signal-to-noise ratio (SNR) estimation. A slight increase in the output signal was observed by increasing the bias voltage, which was associated with an increase in the noise level. Cooling down the detectors reduces their noise and shifts the cutoff wavelength to shorter values. Further improvement in the design and manufacturing process, by increasing the device gain and lowering its noise level, is necessary to meet the required CO_2 lidar/DIAL specifications.

1. Introduction

Light detection and ranging (lidar) is a remote sensing technique suitable for monitoring and mapping atmospheric species. Among these species, carbon dioxide (CO_2) recently has gained interest as one of the dominant greenhouse gases. Kaiser and Schmidt discussed the problem of the CO_2 natural cycle and the uncertainties in understanding the atmospheric CO_2 budget (ref. 1). The ability to monitor atmospheric CO_2 in the shortwave infrared spectral region has been reported in several publications. Ambrico et al. discussed the sensitivity of both 1.6- and 2-μm differential absorption lidar (DIAL) measurements and emphasized the advantage of the 2-μm wavelength (ref. 2). Ismail et al. simulated CO_2 measurements by using the same technique (refs. 3 and 4), and Taczak and Killinger showed attempts for detecting CO_2 using 2 μm (ref. 5). Currently, at NASA Langley Research Center, research is focused on the development of differential absorption lidar (DIAL) technology for CO_2 measurements at the 2-μm wavelength (refs. 3 and 4).

Among the different components of the lidar/DIAL system, the receiver optical detector is of special interest. The detector converts the optical power of the lidar return signal into an electrical signal, thereby directly affecting the instrument measurement sensitivity (ref. 6). Being the dominant noise source in the lidar instrument, the detector affects the system minimum detectable signal and correspondingly the minimum detectable concentration at a certain range (ref. 7). These issues drive the need for a detector of narrow spectral bandwidth, high quantum efficiency, and low noise. Small area avalanche photodiodes (APDs) are an attractive solution for lidar receivers due to their internal gain mechanism and relatively low noise.

Although 2-μm APDs are commercially unavailable, simulation showed that for successful lidar/DIAL measurements, a detector noise equivalent power (NEP) level in the range of 10^{-14} W/Hz$^{1/2}$ is necessary with 55 percent quantum efficiency and at least a 300-μm diameter of the active area (ref. 4). Responsivity as high as 50 A/W, narrow spectral bandwidth, and room temperature operation are further advantages

of such a device. In this report we will discuss the characterization of InGaAsSb based detectors for 2-μm applications. These devices were manufactured by AstroPower, Inc. (Newark, DE) using a prototype APD structure with separate absorption and multiplication regions (SAM). The experimental work was completed to investigate these devices against the CO_2 lidar/DIAL measurement requirements.

1.1. Lidar/DIAL Techniques

The lidar technique uses a pulsed laser source tuned to an absorption feature of an atmospheric species. A collocated receiver telescope collects part of the atmospheric backscattered radiation, which results in density measurements of the constituent as a function of range. The scattering lidar equation used to correlate the transmitted laser power $P(r)$ and the constituent number density $N(r)$ as a function of the range r has the form

$$P(r) = P_o \frac{c\tau A \eta_r \beta(r)}{2r^2} \exp\left\{-2 \int_0^r \left[\sigma N(r) + \kappa(r)\right] dr\right\} \tag{1}$$

where P_o is the initial transmitted power, c is the speed of light, τ is the laser pulse duration, A is the telescope receiver area, η_r is the receiver efficiency, $\beta(r)$ is the atmospheric volume backscatter coefficient, σ is the absorption cross section of the molecular species, and $\kappa(r)$ is the atmospheric extinction coefficient (refs. 7–9).

Because the absorption profile is a unique characteristic for each molecular species, the DIAL technique can distinguish and monitor different atmospheric species such as CO_2. In the DIAL technique, two laser pulses are transmitted successively through the atmosphere. The first is tuned to a strong absorption feature of the species (on-line) and the other is tuned to a weak or no absorption spectral region (off-line). Assuming the two wavelengths are spectrally close (≈100 pm), the atmospheric attenuation and scattering will be equal for both wavelength pulses. Applying equation (1) to both the on- and off-line conditions and solving for the number density yields

$$N(r) = \frac{1}{2(r_2 - r_1)(\sigma_{on} - \sigma_{off})} \ln\left[\frac{P_{off}(r_2) P_{on}(r_1)}{P_{off}(r_1) P_{on}(r_2)}\right] \tag{2}$$

where the subscripts off and on are for the off-line and on-line wavelengths, respectively, $(r_2 - r_1)$ is the measurement range cell, and $(\sigma_{on} - \sigma_{off})$ is the differential absorption cross section (ref. 9).

The optical detector at the lidar receiver telescope output is used in conjunction with a transimpedance amplifier (TIA) to convert the collected radiation power into a voltage V according to

$$V(t) = R_f \cdot \Re(\lambda, V_B, T) \cdot P(r) \tag{3}$$

after correcting for the signal background, where R_f is the TIA feedback resistance and $\Re(\lambda, V_B, T)$ is the detector responsivity, which is a function of the operating wavelength λ, the detector operating bias voltage V_B, and temperature T. The time dependence of equation (3) is converted into spatial (range) dependence by using the speed of light in the relation (ref. 10; to be published).

$$r = \frac{c \cdot t}{2} \tag{4}$$

The factor 2 in the above equation accounts for the round-trip time for the transmitted and the collected backscattered radiation, respectively. Substituting equation (3) into equation (2), the number density can be evaluated directly from the detected signals and will be given by

$$N(t)=\frac{1}{c(t_2-t_1)(\sigma_{on}-\sigma_{off})}\ln\left[\frac{V_{off}(t_2)V_{on}(t_1)}{V_{off}(t_1)V_{on}(t_2)}\right] \tag{5}$$

The DIAL technique can be applied to many atmospheric species, provided that suitable laser sources and detectors are available. Besides CO_2 lidar atmospheric measurements, the 2-μm wavelength is also suitable for water vapor, wind, and cloud measurements.

1.2. InGaAsSb Detectors Overview

InGaAsSb is a promising semiconductor material for developing 2-μm APD detectors. Several articles have discussed the properties of this kind of device using SAM structure (refs. 11–20). The avalanche multiplication process in InGaAsSb material was studied by Andreev et al. (ref. 11). Multiplication factors of 10–20 and 50–100 were achieved at 296 K and 78 K, respectively. Electron and hole impact ionization coefficients were evaluated, and their empirical formulas were given as a function of the electric field (ref. 12). An ionization ratio (defined by the ratio of electron to hole ionization coefficients) up to 60 was reported (ref. 13). Unlike silicon APDs, it was found that holes dominate the impact ionization process, which leads to a relatively higher device noise (ref. 14; to be published). The relation between the impact ionization coefficients and the excess noise factor was also discussed (ref. 12). The same group studied a GaInAsSb/GaAlAsSb SAM APD structure and examined the avalanche breakdown by studying the reverse bias part of the voltage-current characteristics (V-I) at different temperatures. The variation of the spectral response profile with the bias voltage was also given. It was observed that the spectral response peak shifts toward longer wavelengths with higher voltage (ref. 15). Generally, the InGaAsSb material structure was found to have high dark current with mA range damage threshold.

Benoit et al. emphasized the constraints of the value and profile of the electric field for fast and sensitive devices and discussed dark current reduction (ref. 16). Voronina et al. studied the mobility of the charge carriers and its dependence on the doping type and concentration and on the device temperature in InGaAsSb material (ref. 17). Development of InGaAsSb p-n and SAM APD structures were discussed by Shellenbarger et al. (refs. 18–20). Different characteristics were reported, based on frontal and backward illumination of the devices. A backward illuminated p-n junction had a narrow spectral band centered near 2 μm, which has the advantage of reducing the background signal and increasing the detector dynamic range. Several other results were reported for p-n and PIN junctions of the same material (refs. 21–24). These structures have lower noise and higher speed compared to APDs (ref. 25). Table 1 summarizes the detectivity (D^*) measurements of some of these detectors as well as their quantum efficiency. By using the reported area, the NEP can be estimated as given in the table. Besides being under development, none of the reported devices meet the 2-μm CO_2 lidar/DIAL requirements (refs. 3 and 4).

1.3. Detectors' Structure and Operation

A schematic of the SAM APD structure is shown in figure 1. The SAM structure mainly consists of an absorbing narrow bandgap InGaAsSb layer grown on a GaSb substrate, followed by a wide bandgap *n* and p^+AlGaAsSb multiplication layers. Separation of the absorption and multiplication layers helps produce high gain with relatively lower dark current (refs. 13, 15, 16, 18, and 20). The absorption layer width is relatively larger than the multiplication layer, which increases the photon absorption probability and enables the photo-generated charge carriers to reach their optimum velocity corresponding to the

maximum kinetic energy. On the other hand, the multiplication layer has a relatively higher electric field, which increases the impact ionization probability for releasing additional charge carriers that lead to the device internal gain.

The design constraints of the SAM structure were summarized by Benoit et al. as listed in the following: (1) The maximum value of the multiplication region electric field must be greater than 2.7×10^5 V/cm in order to generate an efficient multiplication; (2) for the carriers to reach their optimum velocity and corresponding maximum energy, the absorption layer must be fully depleted, and its depth should be at least twice the absorption length; (3) the electric field at the absorption-multiplication interface should be higher than 5×10^4 V/cm to avoid charge carrier pileup; and (4) the multiplied dark current must be minimized. An additional window layer can be added to the radiation entry side for enhancement of the surface reflection coefficient. Also, a back reflective layer allows the unabsorbed photons to reenter the device, increasing the absorption probability. Generally, InGaAsSb SAM APDs are expected to have higher gain and higher noise compared to InGaAsSb p-n and PIN diodes (ref. 16).

2. Experimental Setup

An experimental setup was assembled to characterize the prototype InGaAsSb detectors considered in this research study. The setup was designed to control the operating conditions of the test detector in terms of bias voltage and temperature and to apply a well-defined optical signal. Also, this setup acquires the detector V-I characteristics, spectral response calibration, and dark noise measurement. Appendix A lists the instruments used to assemble this setup.

Figure 2 shows a schematic of the setup instrumentation and arrangements (refs. 10, 26, and 27). The optical section was designed to apply stable and uniform monochromatic radiation onto the detector in the 1- to 3.2-μm spectral range. The electrical section primarily measures the detector output while controlling its bias voltage and temperature. To minimize calibration errors, the setup has to accommodate for switching between the test and reference detectors with a minimal change in the optical signal and with minimal misalignment. An optical microscope was used to align both the reference and test detectors at the same position with respect to the optical axis and the radiation source (refs. 10, 26, and 27). The microscope had a 15X and 10X eyepiece and objective lenses, respectively, with a 9.5° field of view and a 15.6-mm objective distance.

The investigated detectors were calibrated by using a 3×3 mm^2 PbS reference detector and applying the substitution method, which is discussed in section 4.1. The reference detector was calibrated in the 1- to 3.2-μm spectral range, with 100 nm steps, as shown in figure 3. The estimated uncertainty in the reference detector transferred calibration is 1.0 percent for wavelengths up to 2.5 μm and 1.5 percent for longer wavelengths. Another single point calibration was obtained at 1300 nm, relative to a National Institute of Standards and Technology (NIST) calibrated Ge detector (ref. 28).

2.1. Optical Setup

A quartz halogen lamp, operated by a stabilized current supply, was used as the radiation source. An optical chopper was used to modulate the radiation at 167 Hz (prime number frequency was selected to minimize pickup noise). A monochromator separated the radiation into its spectral components. The monochromator slit-widths were set to 1.25 mm, and two gratings were switched according to the scan wavelength range. High-pass optical filters were installed at the monochromator outlet to block the higher order dispersion of the shorter wavelengths (refs. 26 and 27). The grating and filters cut on wavelength as a function of the scanning wavelength and the corresponding spectral resolution are given in table 2.

Beam-steering optics increased the optical path to collimate the radiation incident on the detector. Additional optics, such as diffusers and neutral density filters, were installed to further condition the radiation. The scan step size was selected to be 40 nm, equivalent to the setup maximum resolution (ref. 29).

The monochromator grating was tested by using an infrared laser source (appendix A). The narrow line width (less than 1 pm) and precise line location (2.051 μm) of the laser allow checking of the monochromator transfer characteristics and spectral calibration, as shown in figure 4. In this experiment, the slit-widths were set to a 0.5-mm equivalent to a resolution of 4 nm up to 2050 nm and 16 nm for a wavelength larger than 2050 nm. The scan was obtained between 2000 and 2100 nm with 5-nm steps. The asymmetry between the left and right portion from the peak is due to the change in the scan resolution for the different gratings.

2.2. Electrical Setup

The TIA circuit used for the detector's current-to-voltage conversion is shown in figure 5 (refs. 14 and 30). A low-noise operational amplifier was used to build this circuit (ref. 31). Resistor R is used to limit the detector current. Also, R associated with the capacitor C acts as a low-pass filter to block high-frequency noise in the detector bias voltage. For zero bias voltage operation, both the resistor and capacitor were removed from the circuit. The feedback resistor R_f defines the current-to-voltage conversion gain according to

$$V = -R_f \cdot I_S \tag{6}$$

where I_S is the detector output current. The TIA and the detector were mounted on a small printed circuit board (PCB) that is installed inside a chamber (refs. 10, 26, 27, and 32). The total noise contribution of the TIA circuit was estimated to be 1.4×10^{-12} A/Hz$^{1/2}$ referred to the output (refs. 14, 30, and 31). Table 3 lists the noise contribution for each circuit component as estimated at room temperature. A stable high-voltage power supply biased the APD, and a ±15-V power supply was used to bias the TIA. A drawback of this circuit arises from the dc offset at the output due to the detector dark current that saturates the operational amplifier. In this case, the TIA is replaced by a low-noise current preamplifier (appendix A) that injects a countercurrent that balances the detector dark current.

The TIA output was connected to an amplifier support module (ref. 29) that further amplifies the signal. The ac coupling was used to eliminate the dc voltage component that resulted from the detector dark current and amplifier offset. A lock-in amplifier was used to measure the detected signal peak-to-peak value, and an oscilloscope was used to check the signal variation. A personal computer (PC) sent commands to the monochromator to adjust the grating position that sets the wavelength for the spectral scan. The PC also acquired the lock-in amplifier reading at every scan step, adjusted the chopping frequency, and supplied synchronizing signals to the other instruments.

2.3. Detector Chamber

Figure 6 shows the assembly diagram of the detector chamber (ref. 32). The chamber is designed to control the detector operating environment and provide a mechanical mount for alignment. Two thermoelectric coolers (TEC) cool the detector mounting plate. The chamber wall acts as a heat sink for the TEC, and water circulation at the chamber back plate dissipates the heat. A refrigerated recirculator provides water circulation at 4 °C. Nitrogen purging prevents water vapor condensation and ice formation on the detector window at low temperatures and also prevents dust accumulation inside the chamber. Detector temperature is monitored by a calibrated thermistor, which is located on the mounting plate as

close as possible to the detector. A temperature controller is used to control the TEC operation and also to provide a temperature readout (ref. 32). This configuration allows cooling down the detector to –20 °C, with 0.1 and 0.01 °C temperature setting and readout resolutions, respectively. The chamber was located on a three-axis translation stage for alignment purposes.

3. V-I Characteristics

The V-I characteristic is a relation between the detector current and its applied bias voltage. The characteristic shifts down by illuminating the device, satisfying the equation (refs. 25 and 33)

$$I = -I_S + I_d = -I_S + I_o\left[\exp\left(\frac{qV_B}{KT}\right) - 1\right] \tag{7}$$

where I is the detector total current, I_d is the detector dark current, I_o is the saturation dark current, q is the electron charge, V_B is the detector bias voltage, K is Boltzmann's constant, and T is the operating temperature. The detector current component that corresponds to the input radiation I_S is given in terms of the detector responsivity and incident optical power P in the relation

$$I_S = \Re(\lambda, V_B, T) \cdot P \tag{8}$$

The V-I characteristic is particularly important near detector breakdown because varying the temperature can identify the breakdown mechanism. The breakdown voltage decreases by decreasing the temperature for the avalanche breakdown mechanism (ref. 33); therefore, by obtaining the reverse branch of V-I characteristics and observing the breakdown behavior, we can distinguish whether the detector is an APD or a regular photodiode (refs. 20 and 33).

The V-I curves were obtained for the detectors under study by using a modular dc source/monitor. Although the manufacturer did not specify the breakdown voltage, the measurements were nondestructive, as was examined by reproducing low-voltage results before and after increasing the bias voltage to near the breakdown level. The voltage scan starts at 100 mV forward bias, with a step of 10 mV toward the reverse bias. The reverse bias was selected carefully to limit the device current to 100 μA. Figure 7 shows the V-I characteristics of four different InGaAsSb samples at three different temperatures and three samples at room temperature. A general observation for this material structure is the increase in the dark current (abrupt in some cases) with reverse bias voltage, which reduces the dynamic range of the detector. The current limit was exceeded for the detector D19-K204-11#6 (fig. 7(d)) up to 500 μA, corresponding to a power consumption of 12.9 mW at 20 °C for power rating investigation. Cooling down this device to –20 °C reduces the dark current, leading to a lower power consumption of 6.5 mW. None of the examined devices showed avalanche behavior, as is clear from the divergence of the V-I curves at higher voltage and different temperatures. These results lead to the conclusion that none of the tested devices was an APD.

4. Spectral Response Calibration

The spectral response is a relation between the detector responsivity in A/W or V/W and the wavelength of the incident optical signal at constant bias voltage and temperature. Generally, the detector responsivity is directly proportional to the incident wavelength up to a point at which it begins to roll off. Ideally, the roll-off is sharp and exists at a wavelength corresponding to the bandgap energy of the semiconductor material in the absorption layer (refs. 25 and 34). Referring to equations (7) and (8), detector

responsivity can be determined by measuring the device output current that results from a known optical power. This output current has to be determined (after subtracting the dark current) at constant wavelength, bias voltage, and temperature. Usually, ac coupling is used to eliminate the dark current after modulating the optical signal. Modulation also helps in measuring very low signals with sensitive instruments, such as lock-in amplifiers. Measuring the input monochromatic signal is a complicated task, which requires either a calibrated source or another calibrated reference detector.

4.1. Calibration by the Substitution Method

The calibration of the detectors under test was obtained by using the substitution method. In this method, the spectral response of a calibrated reference detector is transferred to the test detector by comparing the output of both devices with respect to a constant radiation source at a certain wavelength (ref. 35). Referring to equation (8), assuming a radiation source with constant intensity χ (W/m^2), the reference detector output V_r corresponding to this source will be equal to

$$V_r = \Re_r \cdot A_r \cdot \chi \tag{9}$$

where $\Re_r$ is the reference detector responsivity (V/W). If a test detector with unknown responsivity $\Re_t$ (A/W) were to be placed in the same position as the reference detector with respect to the radiation source, the output current I_t would be given by

$$I_t = \Re_t \cdot A_t \cdot \chi \tag{10}$$

assuming that both the bias voltage and the temperature of the test detector are constants. By dividing equation (9) by equation (10) and referring to equation (6), the test detector responsivity will be given by

$$\Re_t = \frac{I_t \cdot R_f}{V_r} \cdot \frac{A_r}{A_t} \cdot \Re_r \tag{11}$$

where A_r and A_t are the reference and test detectors' areas, respectively. It should be noted that the negative sign in equation (6) was neglected due to the ac coupling (i.e., the negative sign will be equivalent to a phase shift of π).

The above equation can be modified to

$$\Re_t = \mathrm{CF} \cdot \frac{I_t \cdot R_f}{V_r} \cdot \frac{A_r}{A_t} \cdot \Re_r \tag{12}$$

where CF is a correction factor. The correction factor accounts for any different measurement conditions between the test and the reference detectors or their setups. In our case, the PbS reference detector has an $A_r = 3 \times 3$ mm^2 active area. The spectral response of this detector, given in figure 2, was obtained by illuminating only a 1.5-mm diameter area of the device (equivalent to A_r') (ref. 28). Since the whole sensitive area of the device is illuminated during the test detectors' calibration, an area correction factor must be considered. Assuming the reference detector sensitive area is uniform, the correction of the reference detector responsivity will be given by

$$\mathrm{CF}_A = \frac{A_r}{A_r'} = \frac{16}{\pi} \tag{13}$$

Finally, the detector quantum efficiency η can be evaluated from the relation

$$\eta = \frac{hc}{q} \cdot \frac{\Re}{G\lambda} \tag{14}$$

where h is Planck's constant, c is the speed of light, q is the electron charge, and G is the detector gain, if any.

4.2. Calibration Results

By using the experimental setup discussed above, the test detectors were calibrated, all with similar operating conditions of 0-V bias at 20 °C temperature. The scan step was fixed at 40 nm with scan limits of 1000 nm to 2400 nm. The data acquisition was set to 0.5- and 1-sec settling and integration times, respectively, for high signal levels and equal settings of 2 sec for lower signal levels. An intensity monitor is needed in such a setup to correct the data for the radiation source output variation. To avoid this problem, a warm-up time of 1 hr for the radiation source was considered to ensure stable operation. Also, the reference detector measured the radiation source intensity before and after setting each of the test detectors. Intensity variation of less than 1 percent was verified before the calibration measurements.

Figure 8 shows the calibration results of the test detectors, assuming a constant diameter of the sensitive area of 200 μm for all the samples. A cutoff wavelength of about 2.2 μm was observed for all tested devices, which corresponds to the bandgap energy of the composite material $In_{0.15}Ga_{0.85}As_{0.17}Sb_{0.83}$ (ref. 18). Some samples showed a narrower spectral period, corresponding to longer cut-on wavelength (figs. 8(b) and 8(e)), which might be caused by a variation in the InGaAsSb layer thickness that affects the photon absorption depth. The change in the spectral period width was reported for this material structure, and it was explained by the difference between frontal and backward illumination (ref. 18). This narrow spectral period peaks around 2 μm, which is an advantage for the CO_2 lidar/DIAL due to the reduction of the background returns in the absence of a filter. Moreover, detector D13-K203-19#1 showed two separate spectral periods that peaked at about 1 and 2 μm.

It was found that the magnitude of the detectors' responsivity is higher than possible in some cases. This result was investigated by calculating the quantum efficiency by using equation (14) for all the samples, as shown in figure 9, assuming unity internal gain G. Quantum efficiencies higher than 100 percent indicate two possibilities. Either the detectors exhibit some internal gain, or the constant diameter is not a valid assumption for all samples. The second possibility has a higher probability because some of the samples had problems with their contact beside the existence of an epoxy layer on top of the detectors' sensitive area. It was reported that this epoxy layer had caused some problems in the detectors' calibration due to its absorption characteristics around the 2-μm wavelength (ref. 19).

4.3. Spectral Response Variation With Bias Voltage

The detector responsivity is a function of the operating wavelength, bias voltage, and temperature, as indicated in equation (3). At a certain wavelength and operating temperature, the spectral response variation with bias voltage can be investigated by using the substitution method. This method can be applied to the same detector by knowing its calibration because the responsivity is directly proportional to the output

current. As an example, knowing the responsivity at the calibration conditions $\Re_c$, with the calibration bias V_c, the responsivity $\Re_x$, at a different bias V_x, can be obtained from (refs. 10, 26, and 27)

$$\Re(V_x)\big|_{\lambda,T} = \frac{I_x}{I_c} \cdot \Re(V_c)\big|_{\lambda,T} \tag{15}$$

where I_c and I_x are the detector output currents due to the bias voltages V_c and V_x, respectively.

By applying this method, the variation of the detectors' spectral response with the bias voltage was obtained and is shown in figure 10. A room temperature of 20 °C was set for all the detectors. No abrupt increase in the responsivity was observed at higher voltages, which confirms that the samples do not have avalanche gain. Instead, a small increase was observed in some samples, which was associated with relatively higher noise levels. Enhancement of the narrow spectral period between 1.8 and 2.2 μm was seen for the samples D13-K203-19#1 and D19-K204-11#6. These interesting results not only confirm that the detectors exhibit a certain internal nonavalanche gain, but that this gain is selectively applied to a certain part of the detector's spectral range.

4.4. Spectral Response Variation With Temperature

Similarly, at a certain wavelength and operating bias voltage, the spectral response variation with temperature can be investigated by using the substitution method. Knowing the responsivity at the calibration conditions $\Re_c$, with the calibration temperature T_c, the responsivity $\Re_x$, at a different temperature T_x, can be obtained from (refs. 10, 26, and 27)

$$\Re(T_x)\big|_{\lambda,V} = \frac{I_x}{I_c} \cdot \Re(T_c)\big|_{\lambda,V} \tag{16}$$

where I_c and I_x are the detector output currents due to the temperatures T_c and T_x, respectively.

The variation of the detector's spectral response with the temperature is shown in figure 11. Cooling down the detectors leads to a shift in the cutoff wavelength to a shorter value. This result was expected because of the variation in the energy bandgap of the InGaAsSb with temperature (ref. 36). For the detector samples D13-K203-19#1, D15-K204-13#8, and D20-K200-2, the spectral period (1.8 to 2.2 μm) shifts to a shorter value. Away from the spectral period, the three samples showed different behavior with temperature. The responsivity of sample D13-K203-19#1, D15-K204-13#8, and D20-K200-2 had an increase, no change, and a decrease with temperature, respectively.

5. Noise Characterization

Optical detector noise is divided into two types, synchronized and inherent. Synchronized or systematic noise is primarily caused by the electromagnetic and electrostatic interference between the detector and its associated and surrounding circuitry. This type of noise is independent of the detector operation, and it can be reduced successfully by proper grounding, shielding, and differential measurements. Inherent noise is associated with the detector operation and is caused by random processes and can therefore be reduced by averaging. There are several types of inherent noise, the most dominant of which are shot noise, dark current noise, background noise, thermal noise, and 1/f noise (refs. 34, 37, and 38). These noise sources are discussed in the following section.

5.1. Inherent Detector Noise

For an optical detector, shot noise is generated because of the random arrival of the photons that correspond to the optical signal, which leads to random generation of the charge carriers and results in random fluctuation in the detector current. If an internal gain exists, such as in the case of APDs, an additional noise will be contributed due to the randomness in the gain process. This noise is known as the multiplication gain noise. The combined noise effect can be described in the mathematical form

$$\left(i_n^{\text{shot}}\right)^2 = 2qBG \cdot \Re \cdot P \tag{17}$$

where B is the detector bandwidth.

The second term of equation (7) defines the detector dark current, which contributes a dc offset to the detector output. Dark current mainly is due to the thermal generation of charge carriers in the depletion region and their drift due to the existence of the electric field. Both processes are random in nature and independent of the optical signal. Besides, these "dark" charge carriers will be further amplified by the internal gain mechanism; therefore, the dark current noise will be dependent on the dark current and the device internal gain and is given by

$$\left(i_n^{\text{dark}}\right)^2 = 2qBG \cdot I_d \tag{18}$$

Thermal noise (Johnson noise) is caused by the random motion of electrons in resistors. Therefore, every resistor or wire will contribute to this noise, especially the TIA feedback resistor, leading to an increase in the detector's total noise. Johnson noise is given by

$$\left(i_n^{\text{Johnson}}\right)^2 = \frac{4KTB}{R} \tag{19}$$

At low frequency, flicker or 1/f noise is observed in semiconductor materials. This noise is mainly caused by the trap levels within the material bandgap; 1/f noise is given empirically by

$$\left(i_n^{\text{flicker}}\right)^2 = \frac{a}{F^{\alpha}} \tag{20}$$

where F is the operating frequency, α is a constant close to unity, and a is a constant which may depend on the current through the detector and the bandwidth (refs. 35 and 37).

All objects emit blackbody radiation. If this radiation lies in the detector spectral range, the detector will respond to it because it cannot distinguish the signal from this radiation. To the detector, the background will be treated as a "signal" and equation (14) will apply, but with the background signal power P_B. The noise current in this case will be given by

$$\left(i_n^{\text{back}}\right)^2 = 2qBG \cdot \Re \cdot P_B \tag{21}$$

The background power can be estimated from the Stephan-Boltzmann law (ref. 35). Although the background noise is not true inherent noise because it is dependent on the background radiation, it has to be considered since it is associated with the detector operation.

The total detector noise is the power sum of the separate independent noise sources and will be given by

$$I_n\sqrt{B} = \sqrt{\left(i_n^{\text{shot}}\right)^2 + \left(i_n^{\text{dark}}\right)^2 + \left(i_n^{\text{Johnson}}\right)^2 + \left(i_n^{\text{flicker}}\right)^2 + \left(i_n^{\text{back}}\right)^2} \tag{22}$$

where I_n is the detector noise current in A/Hz$^{1/2}$. The measured noise current from the detector circuit, such as that described in figure 5, includes the detector and the TIA circuit noise, I_n^{TIA}. The detector noise can be separated from the total noise I_n^{total} by using the relation

$$I_n = \sqrt{\left(I_n^{\text{total}}\right)^2 - \left(I_n^{\text{TIA}}\right)^2} \tag{23}$$

The TIA noise can be obtained separately by operating the circuit and measuring its noise with the detector replaced by a short circuit. The advantage of this method is that all the synchronized noise from power supplies, instrumentation, and other sources will be included in this measurement.

5.2. Noise Measurement

Using equation (23), the noise spectral density was measured for the test detectors. The measurements were obtained in dark condition by using different bias voltage and temperature settings. At a certain setting, the noise voltage spectral density of the test detectors was measured in conjunction with the TIA circuit by using a spectrum analyzer (appendix A) in the frequency band 1 Hz to 100 kHz, with 1-Hz normalization and 50-kHz center frequency. The noise voltage was then converted to a noise current spectral density using equation (6). The noise spectrum was averaged 1000 times with 50 Ω termination, and the mean value was calculated in the operating frequency band. The TIA noise current was measured associated with the setup and found to be 50×10^{-12} A/Hz$^{1/2}$, with the detector replaced by a short circuit. The net detector noise current was then calculated by subtracting the TIA and setup noise from the total noise measured with the detector.

For the InGaAsSb material structures under investigation, noise increases with increasing device temperature and bias voltage. Figure 12(a) shows the variation of the noise current spectral density with bias voltage obtained at 20 °C. Measurement discrepancy between the different samples was observed and might be caused by poor ohmic contact in the packaging process. Figure 12(b) shows the noise current spectral density variation with temperature obtained at 6- and 15-V bias for detector samples D13-K203-19#1 and D19-K204-11#6, respectively, and 1-V bias for the other samples. Cooling down the detector reduces the noise slightly. Although cryogenic cooling might provide better noise performance, it was not used because of the undefined behavior of the epoxy at low temperatures. It should be noted that the noise results do not include the signal shot noise, since dark condition has been used.

5.3. Noise-Equivalent-Power and Detectivity

Except for the shot noise, the noise sources discussed in section 5.1 are independent of the incident optical power and can be considered constant for certain operating conditions. Shot noise is directly

proportional to the square root of the optical power. The amount of the optical power incident on a detector that produces an output signal that is equal to the noise signal defines the noise-equivalent-power (NEP). In other words, NEP is the optical power that produces a unity signal-to-noise ratio (SNR). For better detector comparison, the NEP is normalized to a bandwidth of 1 Hz and is given by (refs. 34, 37, and 38)

$$\text{NEP} = \frac{I_n}{\Re} \tag{24}$$

The detectivity of a detector (D^*) is an efficient figure of merit when comparing detectors with different areas. The D^* is defined by the reciprocal of the NEP normalized to the detector sensitive area A, and is given by (refs. 34, 37, and 38)

$$D^* = \frac{\sqrt{A}}{\text{NEP}} \tag{25}$$

By characterizing the detector noise currents, the calibration results were used to estimate its NEP and D^*. Figure 13(a) shows the test detectors' NEP variation with wavelength obtained at the calibration conditions. Although the figure indicates the similar noise contents of some of these samples compared to similar devices reported in the literature (table 1), none of the samples was close to the CO_2 DIAL requirement of 2×10^{-14} W/Hz$^{1/2}$ (ref. 4). The large NEP variation between the samples might be caused by the nature of the material composition and/or the different device structures. This fact is consistent with the results of figure 13(b), where D^* is plotted against wavelength for the same detectors.

6. Signal-to-Noise Ratio

The detector power SNR is defined as the square of the signal current (or voltage) divided by the square of the noise current (or voltage). Many factors affect the SNR of an optical detector, including its operating bias voltage and temperature. As discussed earlier, decreasing the temperature of a detector had almost no effect on its responsivity but slightly reduces the noise. Thus, we expect that cooling down the detector will slightly enhance the SNR. On the other hand, increasing the bias voltage increases both the detector responsivity and noise, which might enhance or deteriorate the SNR, depending on the rate by which they individually increase.

Experimentally, SNR can be measured by applying a chopped optical signal to the detector. In this case, the detector output will be similar to the signal shown in figure 14, in which V_d is the dark current component corresponding to the "light off" condition since it is blocked by the chopper blades, and V_s is the signal current corresponding to the "light on" condition. The peak-to-peak optical signal, V_{pp}, is defined as

$$V_{pp} = \overline{V_s} - \overline{V_d} \tag{26}$$

Therefore, the power signal-to-noise ratio will be given here with respect to the rms or the standard deviation of the signal, std (V_s):

$$\text{SNR} = \left[\frac{V_{pp}}{\text{std}(V_S)}\right]^2 \tag{27}$$

Figure 15 shows the variation of the SNR with the bias voltage and temperature, obtained at 2-μm wavelength by using constant source radiation for the two detector samples, D20-K200-2 and D19-K204-11#8. Enhancement of the SNR with decreasing temperature was observed for both devices. On the other hand, SNR deteriorated with increasing bias voltage.

7. Concluding Remarks

The InGaAsSb material structure is a good candidate for 2-μm CO_2 lidar detection. This report presents the characterization results of prototype InGaAsSb detectors near the 2-μm wavelength region. The characterization experiments include voltage-current (V-I) measurements, spectral response and its variation with bias voltage and temperature, noise measurements, noise-equivalent-power (NEP) and detectivity calculations, and signal-to-noise ratio (SNR) estimation. The results were not repeatable for all the characterized detector samples. The temperature dependent V-I measurements indicated the detectors' relatively high dark current, which decreases with temperature. No avalanche behavior was observed near the detector breakdown. Spectral response measurements indicated that an optimization occurred in some detectors around the 1.8- to 2.2-μm spectral region and peaked at 2 μm. All samples showed a cutoff wavelength of 2.2 μm, with different cut-on wavelengths. Quantum efficiency calculations indicated higher responsivity measurements in some spectral ranges, which might be caused by a lack of accuracy in determining the detectors' sensitive area. Bias voltage slightly increases the responsivity only in a certain spectral range, thus confirming the absence of avalanche gain for these samples. Cooling the detectors leads to a shift in the cutoff wavelength to shorter values. Noise measurements showed slight improvement in the noise current at lower temperatures. A significant increase in noise took place while biasing the detectors.

Although the estimated NEP was comparable to similar, previously reported devices, the CO_2 DIAL system requires 2×10^{-14} $W/Hz^{1/2}$, which is about two orders of magnitude lower than the estimated values. Thus, none of the detector samples is suitable for this application. Extensive research efforts are required to improve the performance of the InGaAsSb detectors for DIAL system applications. These efforts should focus mainly on minimizing the device noise and investigating the internal gain mechanism that increases the signal level with bias voltage.

Appendix A

Instrumentation

The instruments used for detector characterization are as follows:

Manufacturer	Model number	Description
Boonton	7200	Capacitance meter
Hewlett Packard	4142B	Modular dc source/monitor
Stanford Research Systems	SR 785	2-Channel dynamic signal analyzer
Agilent Technologies	54845A	Infiniium oscilloscope
Optronics Laboratories, Inc.	750-75MA	Detector enclosure
Optronics Laboratories, Inc.	750-S	Monochromator
Optronics Laboratories, Inc.	740-20 D/IR	IR/Visible dual source attachment
Optronics Laboratories, Inc.	750-HSD-340	PbS detector head
Optronics Laboratories, Inc.	DSM-2B	Detector support module
Optronics Laboratories, Inc.	65A	Programmable current source
Optronics Laboratories, Inc.	750-C	Data acquisition and controller
Hewlett Packard	E3632A	DC power supply
Agilent Technologies	E3631A	Triple output power supply
ILX Lightwave	LDC-3742B	Laser diode controller
ILX Lightwave	LMD-4412	Laser diode mount
Wavelength Electronics	LFI-3751	Temperature controller
Neslab	CFT-25	Refrigerated recirculator
Fluke	51II	Thermometer
Hewlett Packard	E2373a	Multimeter
Stanford Research Systems	SR570	Low-noise current preamplifier
CLR Photonics, Inc.		PZT METEOR single frequency laser

References

1. Kaiser, J.; and Schmidt, K.: Coming to Grips With the World's Greenhouse Gases. *Science*, vol. 281, 1998, pp. 504–506.

2. Ambrico, P.; Amodeo, A.; Girolamo, P.; and Spinelli, N.: Sensitivity Analysis of Differential Absorption Lidar Measurements in the Mid-Infrared Region. *Appl. Opt.*, vol. 39, no. 36, 2000, pp. 6847–6865.

3. Ismail, S.; Browell, E.; Barnes, J.; Koch, G.; Hair, J.; and Singh, U.: Studies Toward the Development of a Space-Based 2-μm Lidar System for Profiling Atmospheric CO_2. *International Geoscience and Remote Sensing Society Symposium*, IGARSS2001, Sydney, Australia, July 2001.

4. Ismail, S.; Koch, G.; Browell, E.; Singh, U.; Abedin, N.; Yu, J.; and Hair, J.: A 2-Micron DIAL System for Profiling Atmospheric CO_2 Lidar Remote Sensing in Atmospheric and Remote Sciences. *21st International Laser Radar Conference*, Quebec City, Canada, 2002.

5. Taczak, T.; and Killinger, D.: Development of a Tunable, Narrow-Linewidth, cw 2.066 μm Ho:YLF Laser for Remote Sensing of Atmospheric CO_2 and H_2O. *Appl. Opt.*, vol. 37, no. 36, 1998, pp. 8460–8476.

6. Killinger, D.; and Menyuk, N.: Laser Remote Sensing of the Atmosphere. *Science*, vol. 235, 1987, pp. 37–45.

7. Measure, R.: *Laser Remote Sensing: Fundamental and Applications*. John Wiley & Sons, Inc., 1984.

8. Carswell, A.: Lidar Measurements of the Atmosphere. *Canadian J. of Physics*, vol. 61, no. 2, 1983, pp. 378–395.

9. Higdon, N.; Browell, E.; Ponsardin, P.; Grossmann, B.; Butler, C.; Chyba, T.; Mayo, M.; Allen, R.; Heuser, A.; Grant, W.; Ismail, S.; Mayor, S.; and Cater, A.: Airborne Differential Absorption Lidar System for Measurements of Atmospheric Water Vapor and Aerosols. *Appl. Opt.*, vol. 33, no. 27, 1994, pp. 6422–6438.

10. Refaat, T. F.; Abedin, M. N.; and Singh, U. N.: Spectral Response Measurements of Short Wave Infrared Detectors (SWIR). *International J. of High Speed Electronics and Systems*, to be published.

11. Andreev, I. A.; Afrailov, M. A.; Baranov, A. N.; Mirsagatov, M. A.; Mikhailova, M. P.; and Yakovlev, Yu. P.: Avalanche Multiplication in Photodiode Structures Using GaInAsSb Solid Solutions. *Soviet Technical Physics Letters*, vol. 13, no. 4, 1987, 199–201.

12. Andreev, I. A.; Mikhailava, M. P.; Mel'nikov, S. V.; Smorchkova, Yu. P.; and Yakovlev, Yu. P.: Avalanche Multiplication and Ionization Coefficients of GaInAsSb. *Soviet Physics-Semiconductor*, vol. 25, no. 8, 1991, pp. 861–865.

13. Mikhailova, M. P.; Andreev, I. A.; Baranov, A. N.; Mel'nikov, S. V.; Smortchkova, Y. P.; and Yakovlev, Y. P.: Low-Noise GaInAsSb/GaAlAsSb SAM Avalanche Photodiode in the 1.6-2.5 μm Spectral Range. *Proceedings of SPIE*, vol. 1580, 1991, pp. 308–312.

14. Abedin, M. N.; Refaat, T. F.; and Singh, U. N.: Noise Measurement of III-V Compound Detectors for 2μm Lidar/DIAL Remote Sensing Applications. *International J. of High Speed Electronics and Systems*, to be published.

15. Andreev, I. A.; Afrailov, M. A.; Baranov, A. N.; Mirsagatov, M. A.; Mikhailov, M. P.; and Yakovlev, Yu. P.: GaInAsSb/GaAlAsSb Avalanche Photodiode With Separate Absorption and Multiplication Regions. *Soviet Tech. Phys. Letters*, 1988, pp. 435–437.

16. Benoit, J.; Boulou, M.; Soulage, G.; Joullie, A.; and Mani, H.: Performance Evaluation of GaAlAsSb/GaInAsSb SAM-APDs for High Bit Rate Transmission in the 2.5μm Wavelength Region. *J. of Optical Communication*, vol. 9, no. 2, 1988, pp. 55–58.

17. Voronina, T.; Dzhurtanov, B.; Lagunova, T.; and Yakovlev, Y.: Behavior of Impurities of p-Type GaInSbAs Solid Solutions. *Soviet Physics-Semiconductor*, vol. 25, no. 2, 1991, pp. 171–173.

18. Shellenbarger, Z. A.; Mauk, M. G.; Gottfried, M. I.; Lesko, J. D.; and DiNetta, L. C.: GaInAsSb and InAsSbP Photodetectors for Mid-Infrared Wavelengths. *Proceedings of SPIE*, vol. 2999, 1997, pp. 25–33.

19. Shellenbarger, Z. A.; Mauk, M. G.; Cox, J.; South, J.; Lesko, J.; Sims, P.; Jhabvala, M.; and Fortin, M.: Recent Progress in GaInAsSb and InAsSbP photodetectors for mid-infrared wavelengths. *Proceedings of SPIE*, vol. 3287, 1998, pp. 138–145.

20. Shellenbarger, Z. A.; Mauk, M. G.; Cox, J.; South, J.; Lesko, J.; Sims, P.; and DiNetta, L.: GaInAsSb and InAsSbP Photodetectors for Mid-Infrared Wavelengths. *Proceedings of SPIE*, vol. 3379, 1998, pp. 354–360.

21. Srivastava, A.; DeWinter, J.; Caneau, C.; Pollack, M.; and Zyskind, J.: High Performance GaInAsSb/GaSb p-n Photodiodes for the 1.8-2.3 μm Wavelength Range. *Appl. Phys. Letters*, vol. 48, no. 14, 1986, pp. 903–904.

22. Zhang, B.; Zhou, T.; Jiang, H.; Ning, Y.; and Jin, Y.: GaInAsSb/GaSb Infrared Photodetectors Prepared by MOCVD. *Electr. Letters*, vol. 31, no. 10, 1995, pp. 830–832.

23. Li, A.; Zhong, J.; Zheng, Y.; Wang, J.; Ru, G.; Bi, W.; and Qi, M.: Molecular Beam Epitaxial Growth, Characterization and Performance of High-Detectivity GaInAsSb/GaSb PIN Detectors Operating at 2.0 to 2.6 μm. *J. of Crystal Growth*, vol. 150, 1995, pp. 1375–1378.

24. Andreev, I.; Afrailov, M.; Baranov, A.; Konnikov, S.; Mirsagatov, M.; Mikhailova, M.; Salata, O.; Umanskii, V.; Filaretova, G.; and Yakovlev, Y.: Ultrafast GaInAsSb p-i-n Photodiode for the Spectral Interval 1.5-2.3 μm. *Soviet Technical Phys. Letters*, vol. 15, no. 4, 1989, pp. 253–254.

25. Saleh, B.; and Tiech, M.: *Fundamentals of Photonics*. John Wiley & Sons, Inc., 1991.

26. Refaat, T.; Halama, G.; and DeYoung, R.: Comparison Between Super Low Ionization Ratio and Reach Through Avalanche Photodiode Structures. *Opt. Eng.*, vol. 39, no. 10, 2000, pp. 2642–2650.

27. Refaat, T.; Halama, G.; and DeYoung, R.: *Characterization of Advanced Avalanche Photodiodes for Water Vapor Lidar Receivers*. NASA/TP-2000-210096.

28. Report of Calibration of One High Sensitivity Detector Module OL 750-HSD-340C, Optronics Lab., Inc., 2001.

29. OL Series 750 Automated Spectroradiometric Measurement System. Optronics Lab., Inc., Manual no. M000215, Revis. B, April 2000.

30. Clayton, G.: *Operational Amplifiers*. Butterworth & Co. Ltd., London, 1987.

31. Precision High-Speed Difet Operational Amplifiers. Burr Brown, 1989.

32. LDM-4412 Laser Diode Mount, Instruction Manual. ILX Lightwave Corp., May 1998.

33. Sze, S.: *Physics of Semiconductor Devices*. John Wiley & Sons, Inc., 1981.

34. Dereniak, E.; and Crowe, D.: *Optical Radiation Detectors*. Wiley Series in Appl. Optics, Wiley, New York, 1991.

35. Larason, Thomas C.; Bruce, Sally S.; and Parr, Albert C.: Spectroradiometric Detector Measurements: Part I—Ultraviolet Detectors and Part II—Visible to Near-Infrared Detectors. *NIST Spec. Publ.*, Feb. 1998, pp. 250–41.

36. Yuan, T.; Baolin, Z.; Yixin, J.; Tianming, Z.; Shuwe, L.; Yongqiang, N.; Jinshan, Y.; Hong, J.; and Guang, Y.: Calculation on Relation of Energy Bandgap to Composition and Temperature for $Ga_xIn_{1-x}As_{1-y}Sb_y$. Rare Metals, vol. 15, no. 3, 1996, pp. 172–178.

37. Vliet, K.: Noise Limitations in Solid State Photodetectors. *Appl. Opt.*, vol. 6, no. 7, 1967, pp. 1145–1168.

38. Nudelman, S.: The Detectivity of Infrared Photodetectors. *Appl. Opt.*, vol. 1, no. 5, 1962, pp. 627–636.

Table 1. Different Reported Detectors and Their Parameters: Active Area (A), Detectivity (D^*), Quantum Efficiency (QE), and Wavelength λ

Material structure	A	D^*	NEP	QE	λ	Ref.
	cm^2	$cmHz^{1/2}/W$	$W/Hz^{1/2}$	%	μm	
p−GaInAsSb/nGaSb (p-n)	2.5×10^{-4}	7×10^{9}	2.3×10^{-12}	67 ± 5	2.2	21
p^+GaInAsSb/p^+GaInAsSb/n−GaSb		10^{9}			2.25	22
p^+GaInAsSb/p−GaInAsSb/n^+GaInAsSb/n^+GaSb	1.6×10^{-3} 4×10^{-4} 7.85×10^{-5}	3×10^{9}	1.3×10^{-11} 6.7×10^{-12} 2.9×10^{-12}	65	2.5	22
pGaInAsSb/nGaInAsSb/nGaSb	3.61×10^{-2}	1.85×10^{8}	1.0×10^{-9}			18

Table 2. Gratings and Filters Used as Function of Scan Spectral Range With Corresponding Resolution

Spectral range		Grating grove/mm	Filter cut-on, nm	Resolution FWHM[a], nm
Start, nm	End, nm			
1000	1100	600	602	10
1110	1930	600	1119	10
1940	2040	600	1949	10
2050	3200	150	1949	40

[a]Full width at half maximum.

Table 3. Transimpedance Amplifier (TIA) Circuit Component Values and Noise Contribution

Component	Value	Noise current
R	10 kΩ	1.3×10^{-12} $A/Hz^{1/2}$
C	1 μF	
R_f	50 kΩ	5.7×10^{-13} $A/Hz^{1/2}$
Op amp	OPA627	1.6×10^{-13} $A/Hz^{1/2}$

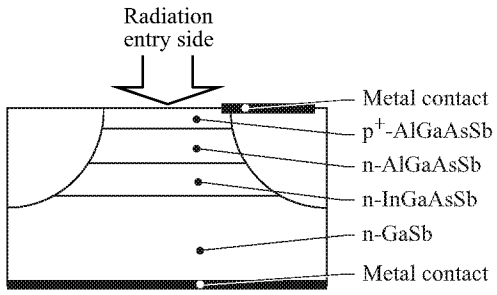

Figure 1. Schematic of InGaAsSb detector structure.

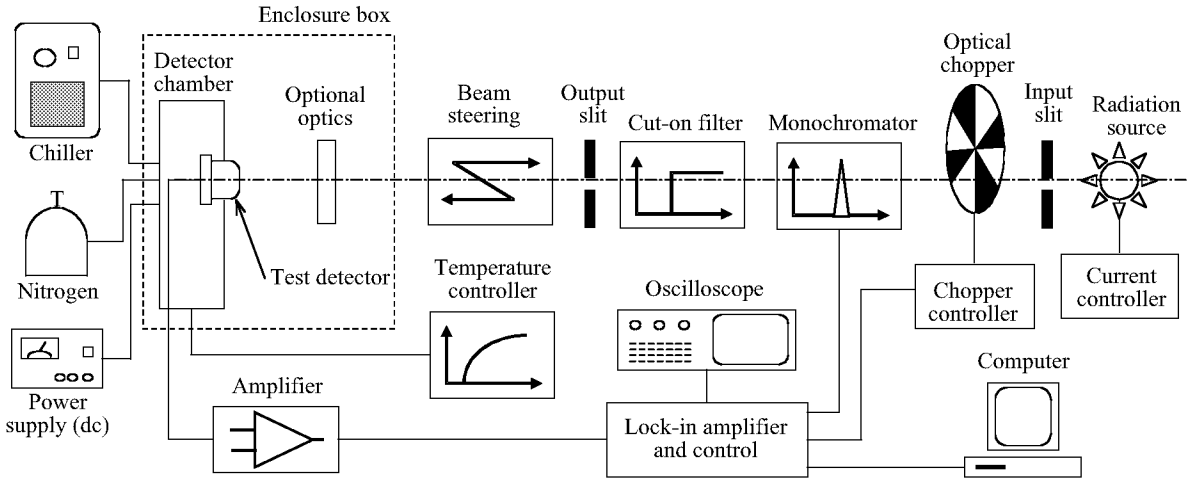

Figure 2. Experimental setup for detector calibration.

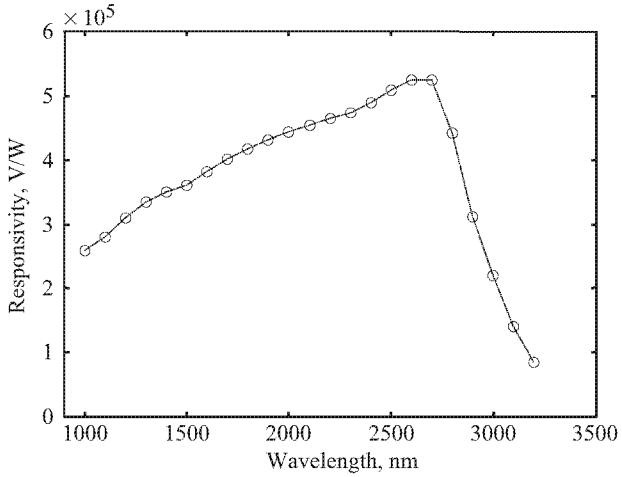

Figure 3. Spectral response calibration of PbS reference detector.

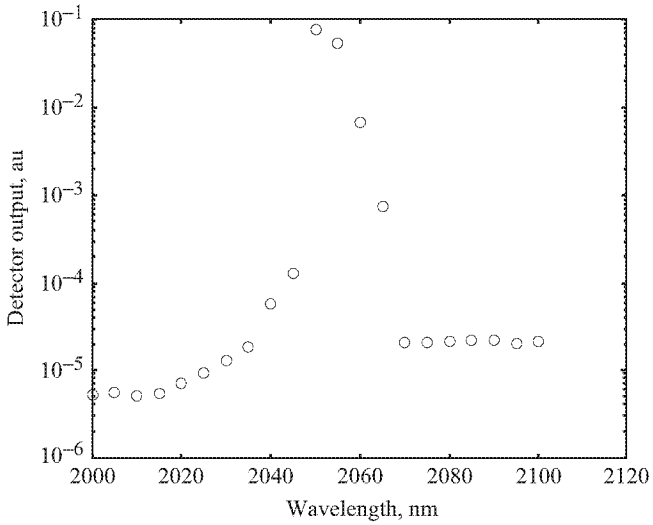

Figure 4. Reference detector output corresponding to 2.051-μm laser source.

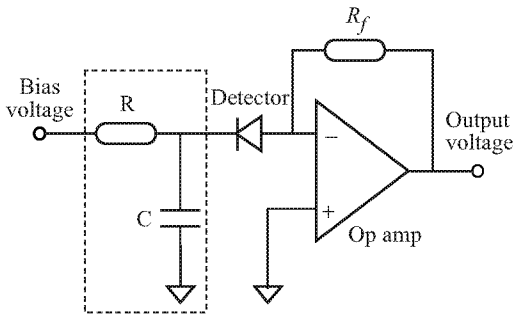

Figure 5. Detector transimpedance amplifier (TIA) circuit.

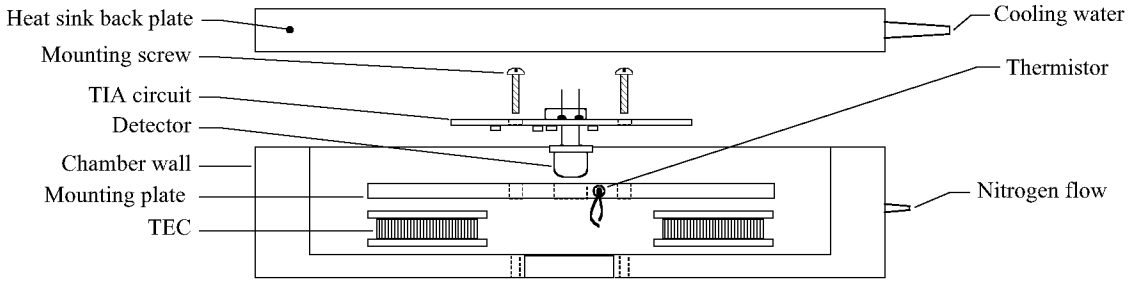

Figure 6. Assembly of detector chamber. (TEC stands for thermoelectric coolers.)

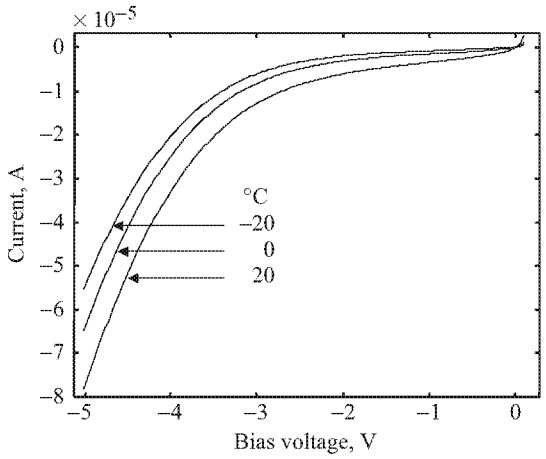

(a) D13-K203-19#1.

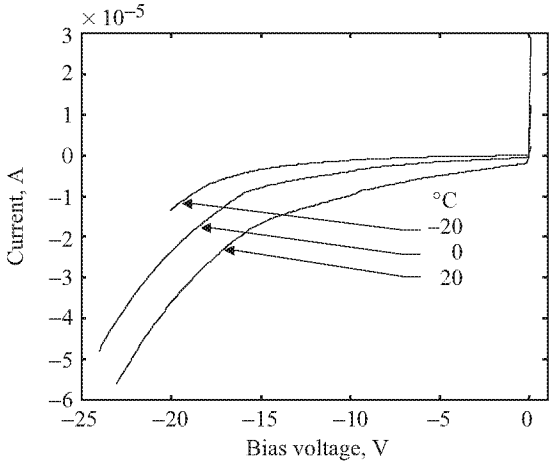

(b) D15-K204-13#5.

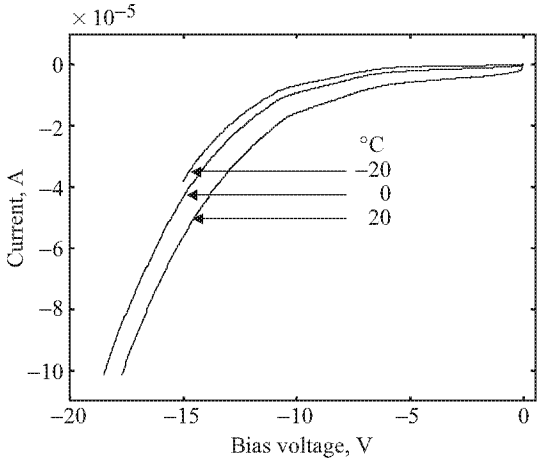

(c) D19-K204-11#3.

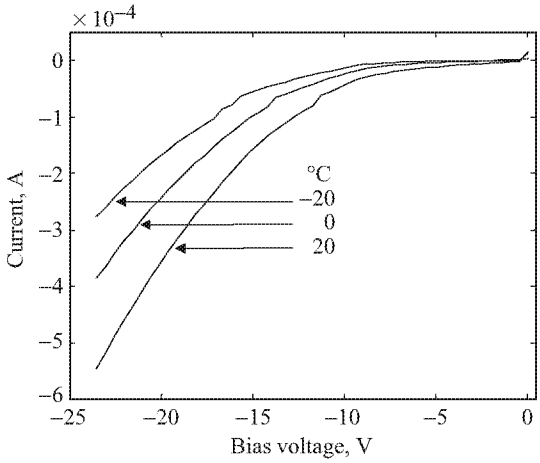

(d) D19-K204-11#6.

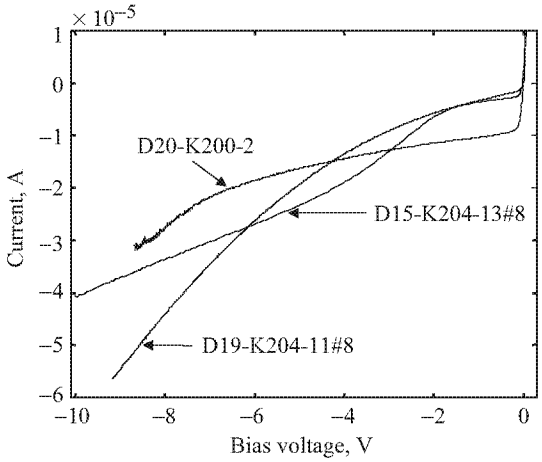

(e) Compares V-I for different samples at 22 °C.

Figure 7. Voltage-current (V-I) characteristics at different temperatures for InGaAsSb detectors.

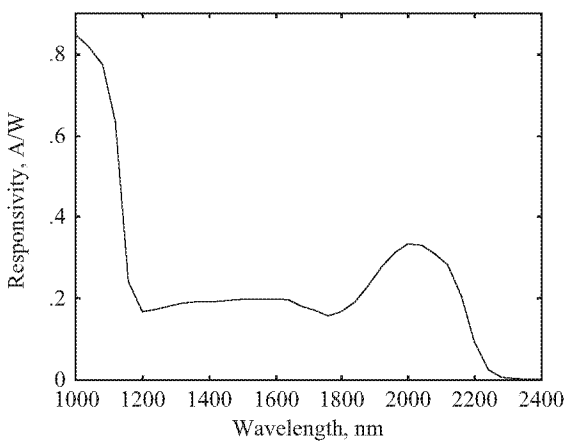

(a) D13-K203-19#1.

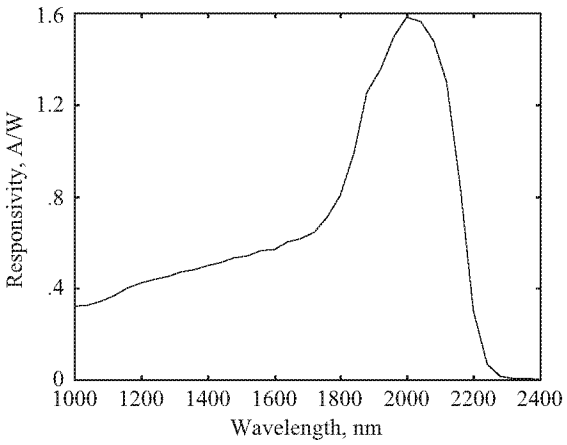

(b) D15-K204-13#8.

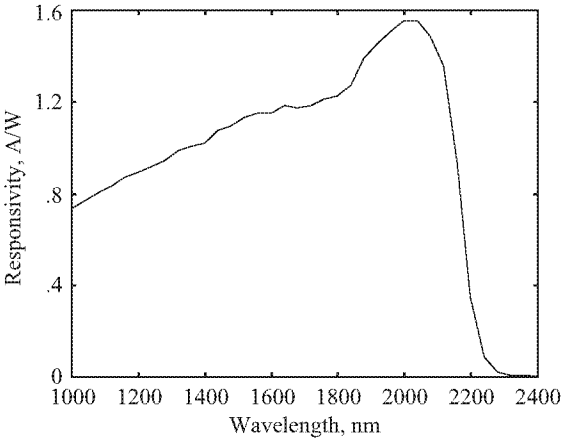

(c) D19-K204-11#6.

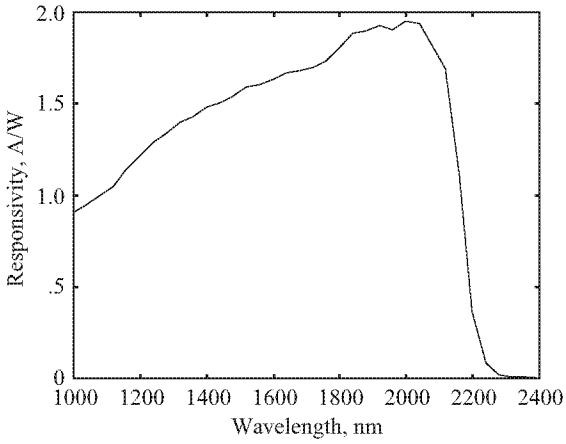

(d) D19-K204-11#8.

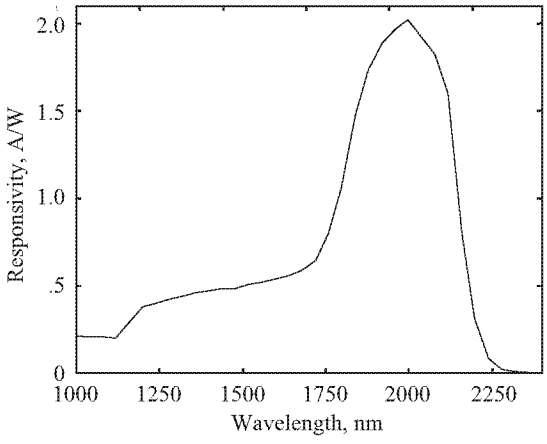

(e) D20-K200-2.

Figure 8. Spectral response calibration of InGaAsSb detectors obtained at 20 °C and 0-V bias voltage.

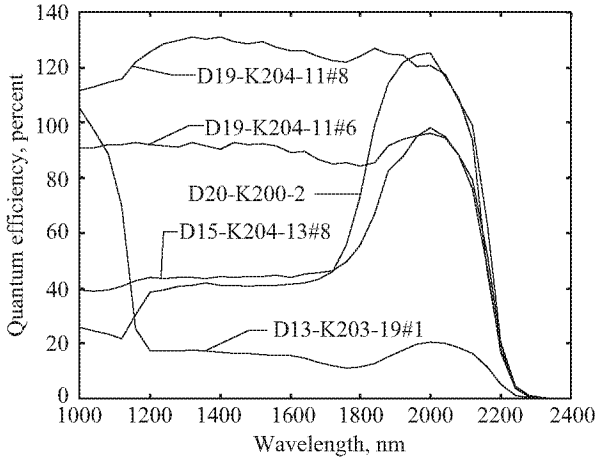

Figure 9. Detectors' quantum efficiency comparison at spectral calibration operating conditions.

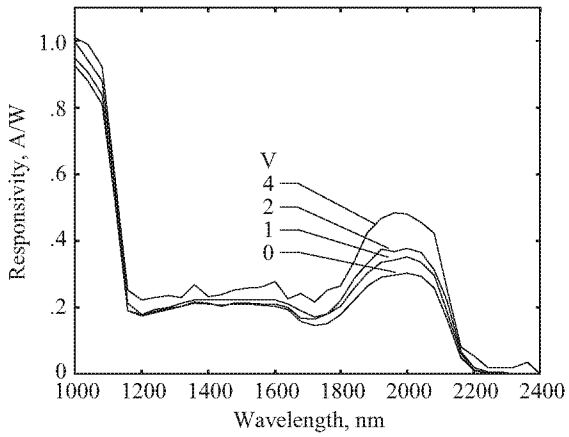

(a) D13-K203-19#1.

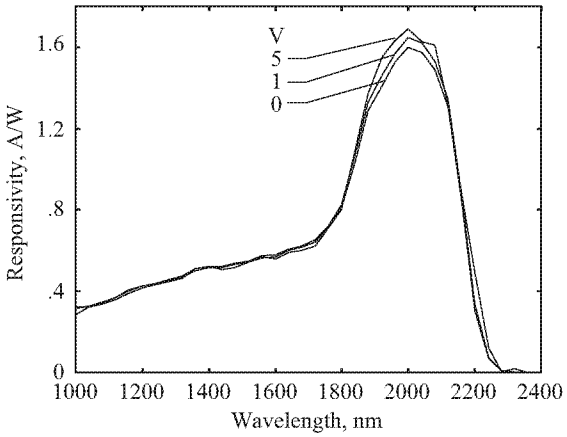

(b) D15-K204-13#8.

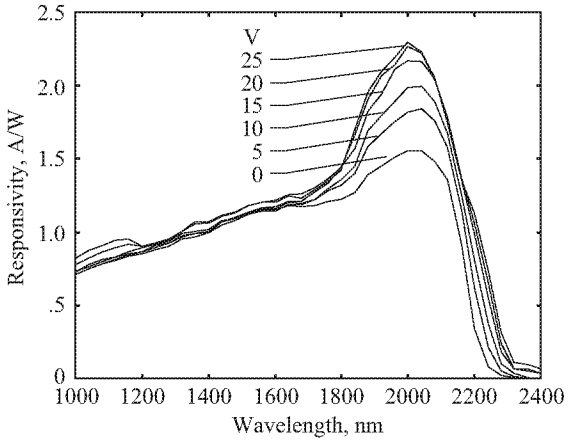

(c) D19-K204-11#6.

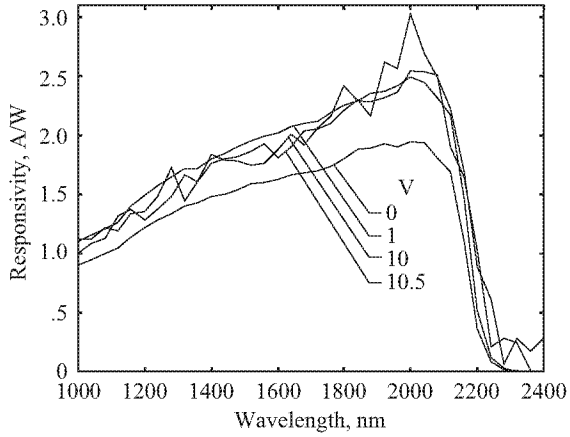

(d) D19-K204-11#8.

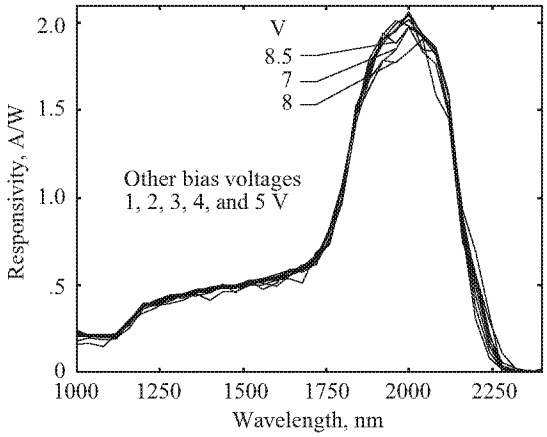

(e) D20-K200-2.

Figure 10. Spectral response variation with bias voltage for InGaAsSb detectors obtained at 20 °C temperature.

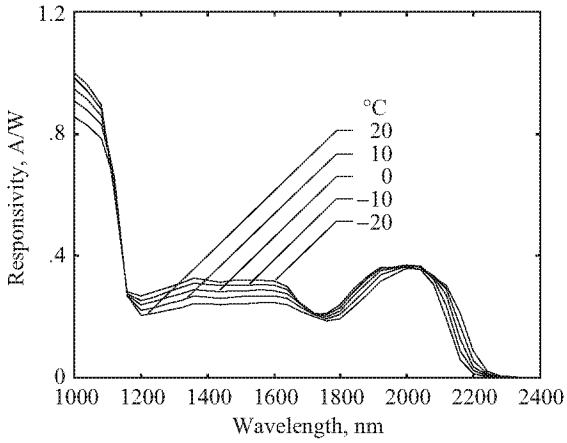

(a) D13-K203-19#1.

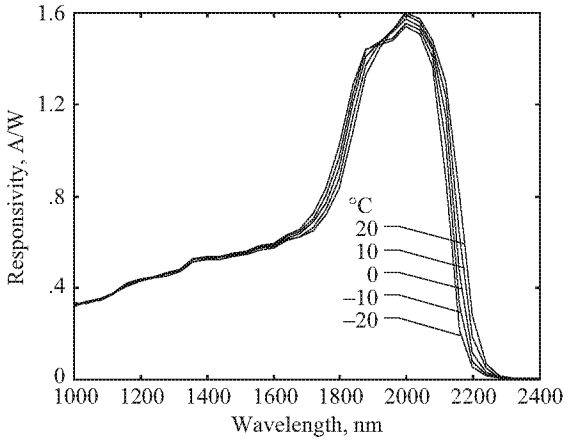

(b) D15-K204-13#8.

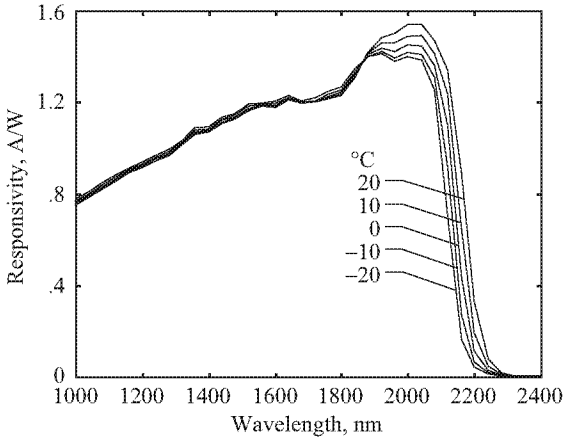

(c) D19-K204-11#6.

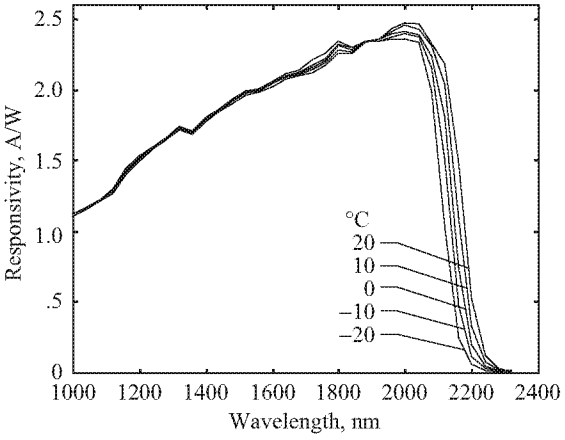

(d) D19-K204-11#8.

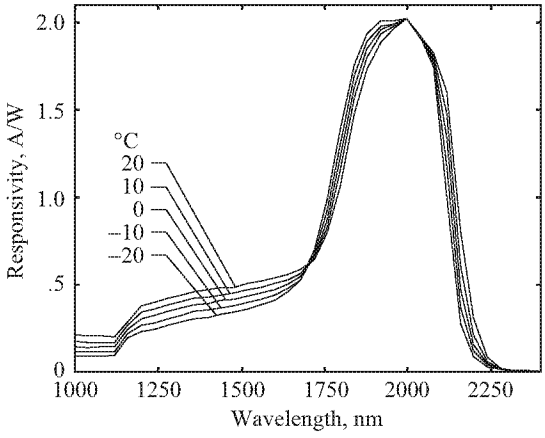

(e) D20-K200-2.

Figure 11. Spectral response variation with temperature for InGaAsSb detectors obtained at 1-V bias voltage.

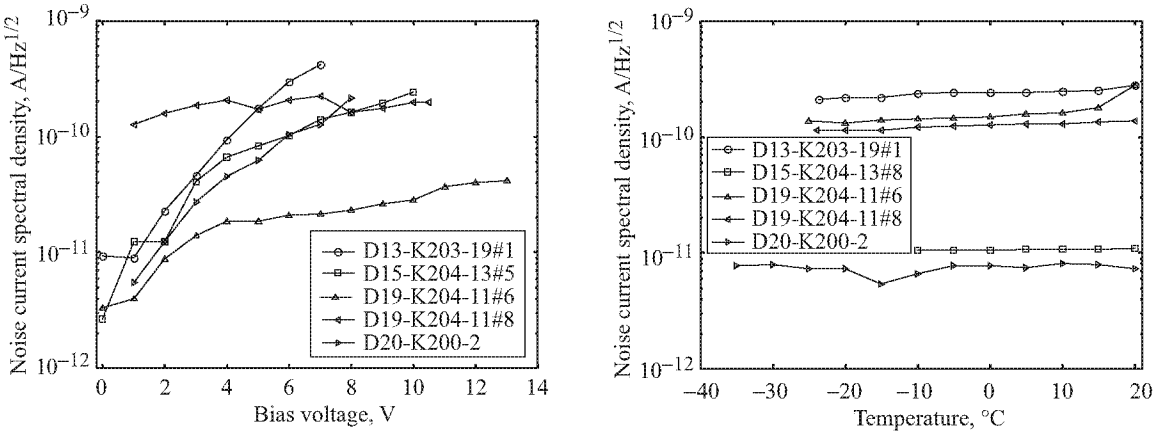

(a) Variation with bias voltage at 20 °C.

(b) Variation with temperature at bias voltages specified in text.

Figure 12. Variation of noise current spectral density.

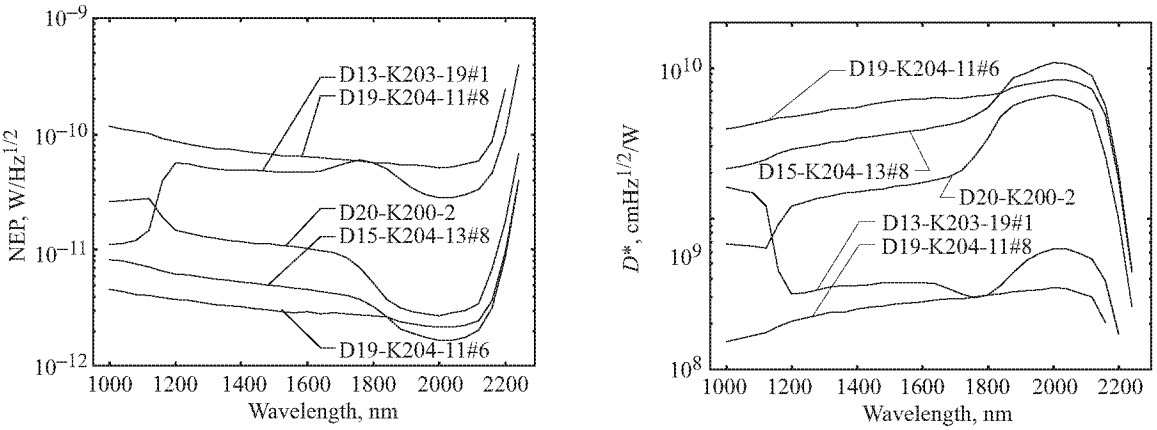

(a) NEP.

(b) D^*.

Figure 13. Noise-equivalent power (NEP) and detectivity (D^*) variation with wavelength at spectral calibration operating conditions.

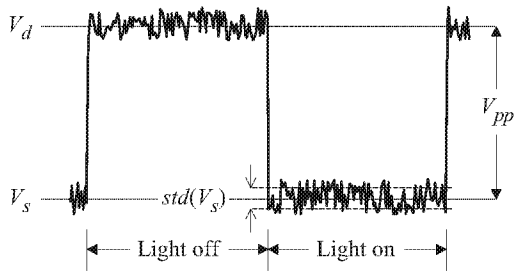

Figure 14. Signal-to-noise ratio (SNR) measurement using optically chopped signal.

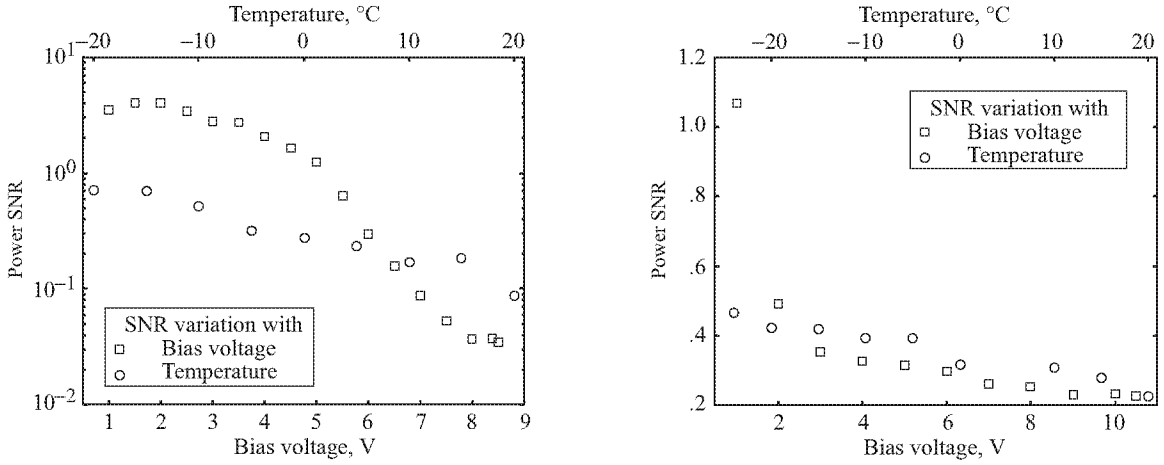

(a) D20-K200-2.

(b) D19-K204-11#8.

Figure 15. Signal-to-noise ratio (SNR) measurements for InGaAsSb detectors. SNR variation with temperature obtained at 1-V bias and SNR variation with voltage obtained at 20 °C.

REPORT DOCUMENTATION PAGE

Form Approved
OMB No. 0704-0188

1. REPORT DATE *(DD-MM-YYYY)*	2. REPORT TYPE	3. DATES COVERED *(From - To)*
01- 02 - 2003	Technical Publication	

4. TITLE AND SUBTITLE

InGaAsSb Detectors' Characterization for 2-μm CO_2 Lidar/DIAL Applications

5a. CONTRACT NUMBER

5b. GRANT NUMBER

5c. PROGRAM ELEMENT NUMBER

6. AUTHOR(S)

Refaat, Tamer F.; Abedin, M. Nurul; Koch, Grady J.; and Singh, Upendra N.

5d. PROJECT NUMBER

5e. TASK NUMBER

5f. WORK UNIT NUMBER

755-09-00-07

7. PERFORMING ORGANIZATION NAME(S) AND ADDRESS(ES)

NASA Langley Research Center
Hampton, VA 23681-2199

8. PERFORMING ORGANIZATION REPORT NUMBER

L-18243

9. SPONSORING/MONITORING AGENCY NAME(S) AND ADDRESS(ES)

National Aeronautics and Space Administration
Washington, DC 20546-0001

10. SPONSOR/MONITOR'S ACRONYM(S)

NASA

11. SPONSOR/MONITOR'S REPORT NUMBER(S)

NASA/TP-2003-212140

12. DISTRIBUTION/AVAILABILITY STATEMENT

Unclassified - Unlimited
Subject Category 33
Availability: NASA CASI (301) 621-0390 Distribution: Standard

13. SUPPLEMENTARY NOTES

Refaat, Science and Technology Corp. Abedin, Koch, and Singh, Langley Research Center.
An electronic version can be found at http://techreports.larc.nasa.gov/ltrs/ or http://techreports.larc.nasa.gov/cgi-bin/NTRS

14. ABSTRACT

Recent interest in monitoring atmospheric CO_2 focuses attention on infrared remote sensing using the 2-μm lidar/differential absorption lidar (DIAL) technique. Quantum detectors are critical components in this technique, and many research efforts concentrate on developing such devices for the 2-μm wavelength. Characterization results of InGaAsSb quantum detectors for the 2-μm wavelength range are presented, including experimental setup and procedure. Detectors are prototype devices manufactured by using separate absorption and multiplication (SAM) structures. Characterization experiments include V-I measurements, spectral response and its variation with bias voltage and temperature, noise measurements, noise-equivalent-power (NEP) and detectivity calculations, and signal-to-noise ratio (SNR) estimation. A slight increase in the output signal occurred with increased bias voltage and was associated with a noise level increase. Cooling down the detectors reduces noise and shifts the cutoff wavelength to shorter values. Further improvement in the design and manufacturing process, by increasing the device gain and lowering its noise level, is necessary to meet the required CO_2 lidar/DIAL specifications.

15. SUBJECT TERMS

Infrared detectors; 2-μm avalanche photodiodes (APDs); InGaAsSb separate absorption and multiplication (SAM) structures; Noise-equivalent power (NEP); Detectivity (D*); Signal-to-noise ratio (SNR)

16. SECURITY CLASSIFICATION OF:			17. LIMITATION OF ABSTRACT	18. NUMBER OF PAGES	19a. NAME OF RESPONSIBLE PERSON
a. REPORT	b. ABSTRACT	c. THIS PAGE			STI Help Desk (email: help@sti.nasa.gov)
					19b. TELEPHONE NUMBER *(Include area code)*
U	U	U	UU	32	(301) 621-0390